Open Ceramics 26 (2026) 100973

Contents lists available at ScienceDirect

Open Ceramics

journal homepage: www.sciencedirect.com/journal/open-ceramics

Additive manufacturing of ceramic matrix composites based on carbon fiber reinforced PEEK by material extrusion technology: Design based deformation mechanisms

Wolfgang Freudenberg [a,*], Felix Werner [a], Max Friedel [b], Nico Langhof [a], Holger Ruckdäschel [b], Stefan Schafföner [a]

[a] University of Bayreuth, Chair of Ceramic Materials Engineering (CME), Prof.-Rüdiger-Bormann-Str. 1, 95447 Bayreuth, Germany
[b] University of Bayreuth, Department of Polymer Engineering, Universitätsstr. 30, 95447 Bayreuth, Germany

ARTICLE INFO

Keywords:
Additive manufacturing (AM)
Material extrusion (MEX)
Process-induced deformation

ABSTRACT

This study explores the deformation mechanisms during the fabrication of carbon fiber reinforced ceramic matrix composites (CMC) using a modified liquid silicon infiltration (LSI) process. Starting from additively manufactured carbon fiber reinforced polymers (CFRP) components based on carbon fiber reinforced polyetheretherketone (CF-PEEK). The processing included thermal crosslinking, pyrolysis, and silicon infiltration. A gear wheel geometry was used to evaluate deformation effects to define four shape stability criteria and finally to predict the deformations. Key factors influencing deformation were identified, including anisotropic fiber orientation, infill density, and thermal crosslinking efficiency. Three distinct deformation categories were determined: unavoidable shrinkage-induced deformation, distortion due to internal stress, and severe shape loss caused by insufficient gas release during pyrolysis. Finite element simulations qualitatively predicted and correlated the deformation behavior with the experimental results. The study demonstrated how optimized slicing strategies and controlled processing can minimize deformation, enabling more reliable and reproducible near-net-shape manufacturing of complex CMC components.

1. Introduction

Ceramic matrix composites (CMC) are fiber-reinforced ceramic materials designed to combine the high-temperature stability of ceramics with enhanced fracture toughness, thermal shock resistance, and load-bearing capability for severe aerospace and other ultra-high-temperature structural applications. They are used when standard materials reach their limits. Typical benefits of CMC include a high hardness, high wear resistance, high temperature stability, high chemical resistance and non-brittle failure behavior [1–5]. The manufacturing, often accompanied by a multi-stage process at high temperatures in combination with elaborate and time-consuming finishing, makes the production of CMC cost intensive. As the machining accounts for up to 25 % of the total costs [6,7], rising with increasing complexity of the component's geometry, it is desirable to pursue near-net-shape production.

The state-of-the-art production processes of CMC start with the manufacturing of carbon fiber reinforced polymers (CFRP), such as resin transfer molding (RTM), warmpressing, vacuum infusion, winding or pultrusion [8–11]. Mostly semi-finished products are used. These include fabrics and non-woven unidirectional laminates, which limit the freedom of design. Due to these limitations, the final machining costs are correspondingly high. Besides this design limitation there is also another point to consider regarding the shape of the final CMC part. During pyrolysis at temperatures up to 1000 °C, the polymer matrix is converted to amorphous carbon, releasing gaseous decomposition products. This can lead to delaminations in the C/C part. Furthermore, this conversion is accompanied by shrinkage. Due to the use of carbon fibers or semi-finished carbon fiber products which hinder the shrinkage [12,13], there is anisotropic shrinkage within the part. This effect results from the conversion of the thermoplastic matrix into amorphous carbon by releasing gaseous decomposition products and by a density increase. Deformation during CMC processing is a significant issue that must be addressed. While matrix shrinkage is an unavoidable process, delamination is an avoidable deformation that should be prevented.

The remelting of the thermoplastic polymer in CFRP causes possible

---

* Corresponding author.
E-mail address: wolfgang.freudenberg@uni-bayreuth.de (W. Freudenberg).

https://doi.org/10.1016/j.oceram.2026.100973
Received 7 April 2026; Received in revised form 7 May 2026; Accepted 8 May 2026

deformation. Furthermore, there are other effects influencing the deformation of the printed parts by material extrusion technology during the conversion process to ceramic matrix composites. One factor is the moisture of the used thermoplastic filament and the influence on the resulting microstructure. Zaldivar et al. showed the microstructure becomes less distinct by increasing content of moisture in the filament. In particular for the subsequent, thermally induced crosslinking of the CFRP parts, a high specific surface area is necessary [14]. A drying step for the filament before printing is therefore recommended.

Another important effect is the shrinkage of the parts during pyrolysis [15]. Indeed, the release of gases during pyrolysis cannot be avoided. Moreover, the use of fiber reinforcement, resulting in an anisotropic shrinkage, makes it more complex to achieve the desired final near-net-shape part. Especially the limitation of fiber reinforcement in the planar x-y-direction during the printing process leads to a higher shrinkage in z-direction during pyrolysis, as no fibers hinder the shrinkage of the matrix. This must be considered in the design of the final geometry [16].

The study primarily investigates the fundamental, design-based deformation mechanisms that occur during the processing chain from additive manufacturing of carbon-fiber-reinforced PEEK to conversion into C/C-SiC via liquid silicon infiltration, using a gear wheel geometry as an exemplary case. Besides the manufacturing, scanning and comparison of the real part and the CAD-model, a FEM-simulation was performed additionally. The results of simulation and scanning enable predictions for the manufacturing of near-net-shape parts.

2. Materials and methods

2.1. Material and test geometry

The applied material was a commercially available carbon fiber reinforced PEEK. The filament was provided by Desktop Metal® and had a diameter of 1.75 mm. The fiber volume content was 16 % and the fiber length was in the range of 50 – 200 μm. Fig. 1 shows the gear wheel that was chosen as the test geometry due to its sufficient complexity and the numerous measurement points available for detecting deformation mechanisms. The diameter of the wheel was set to 75 mm and the height to 8 mm.

2.2. Slicing

The used slicing software was Cura 5.7.1 (Ultimaker). Most parameters were kept constant, as there was no detectable influence on any kind of deformation in the whole process chain. The layer height was set to 0.15 mm, the wall line count was 2, the infill pattern was "lines" with no connection of the lines, printing temperature was 410 °C, the build plate temperature was 50 °C, the printing speed was 25 mm/s and no support structure and no top layer was used. The critical parameters were in general **infill** and **printing direction**. The variation of these parameters is illustrated in Fig. 2. These parameters were varied and parts were printed separately for each parameter combination to investigate the effect on the deformation. Unless otherwise specified, the infill was 80 % and the printing direction was quasi-isotropic $[0°, 90°, 45°, 135°, 60°, 150°, 30°, 120°]_n$. Each gear wheel was crosslinked, as described inSection 2.3, after the printing process except for the bottom-middle one in Fig. 2.

Fig. 1. Gear wheel test geometry.

The schemes of the gear wheels are shown again in the following sections to make it easier to identify the key slicing parameters, regarding the resulting deformation mechanisms.

2.3. LSI-process (liquid silicon infiltration)

The general three-step LSI-process was modified through an additional thermally induced crosslinking step after the CFRP manufacturing. This was necessary due to the use of PEEK as a thermoplastic matrix. An overview of the modified LSI-process is shown in Fig. 3.

2.3.1. CFRP manufacturing

The CF-PEEK filament was dried for 24 h at 75 °C before it was printed. The CFRP manufacturing was carried out by material extrusion (Intamsys Funmat HT Enhanced, China). After the printing process an additional thermally crosslinking step was carried out in a chamber furnace (N60/ HR, Nabertherm GmbH, Germany). This step initiated a partially crosslinking reaction of the printed parts and avoided the remelting during pyrolysis. The thermally induced crosslinking was conducted in static air at 335 °C for 48 h [17]. The heating rate was set to 2 K/min.

2.3.2. Pyrolysis

The CFRP is converted to carbon fiber reinforced carbon (C/C) during pyrolysis. This step was conducted at 1000 °C in a nitrogen atmosphere in a batch furnace (FCT Anlagenbau GmbH, Germany). The conversion of the thermoplastic PEEK matrix into carbon occurred through the release of gaseous decomposition products in combination with anisotropic shrinkage due to the fiber orientation and the hindrance of shrinkage by the fibers. Regarding the manufacturing process, the fibers are aligned in the x-y-direction, resulting in a significantly higher shrinkage in z-direction.

2.3.3. Siliconization

The conversion to a ceramic matrix composite was finalized by the liquid silicon infiltration. The process was carried out at temperatures above 1425 °C in vacuum atmosphere in a batch furnace (FCT Anlagenbau GmbH, Germany). The used silicon was provided by Elkem AS, Norway (Silgrain®HQ, >99.7 wt.-% Si). Silicon infiltrated the porous C/C by capillary forces, reacted with the carbon and finally formed the C/C-SiC parts.

2.4. Dimensional accuracy

The dimensional changes were determined after each process step. The geometry was measured using a caliper (mean value of five height and six diameter points) and by 3D scanning of each part after each process step. The details of the 3D-scan are described in Section 2.7.

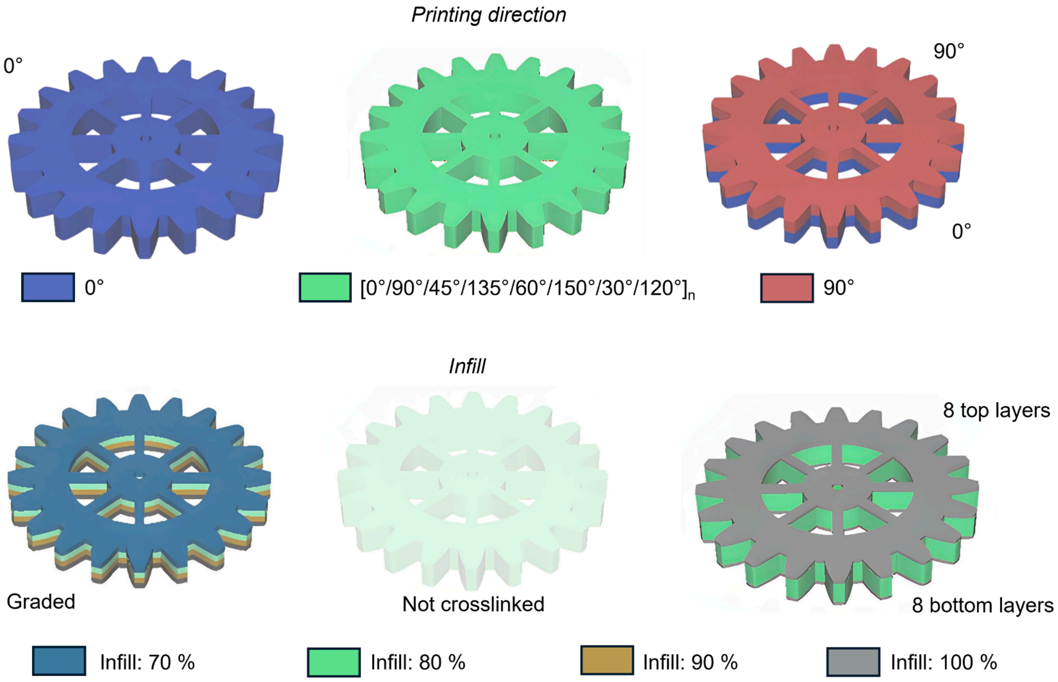

Fig. 2. Parameter variation of the printing direction and the infill, respectively and the resulting differing layer structure of the gear wheel part.

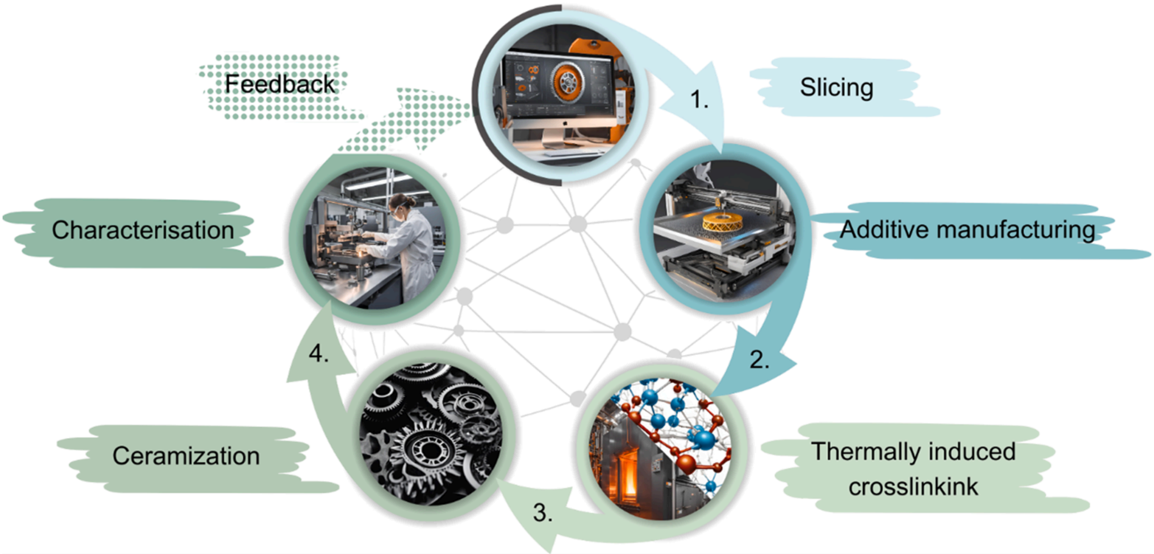

Fig. 3. Modified LSI-process, illustrating the interconnecting network of each process step.

2.5. *Definition of dimensional stability criteria*

Regarding properties and test methods of additive manufactured parts, the standard DIN EN ISO 17,296–3 differs between metals, polymers and ceramics. Moreover, there is a subdivision due to the application of highly developed components (safety-relevant), functional components (not safety-relevant) and prototypes, which are categorized by '+' for fulfillment criteria, 'o' for recommended criteria and '-' for not applicable criteria. In the case of ceramic components and geometric requirements it is referred to DIN EN ISO 129–1, DIN EN ISO 286-1, DIN EN ISO 14,405-1, DIN EN ISO 1938-1, DIN EN ISO 2768-1/2, DIN EN ISO ASTM 52,902 [18–24]. These standards generally cover standard geometries such as drill holes, verticals, fits, shafts, etc., so it was necessary to define our own criteria for this gear wheel geometry, investigated in this study.

The investigation and quantification of deformation mechanisms of especially complex parts required the definition of dimensional stability criteria. The criteria were utilized for the purpose of evaluating the component's conformity with the established deformation tolerances. In this study four different stability criteria were especially defined for the used material, process and geometry of the component by the corresponding author and illustrated for a better understanding. These criteria were introduced in order to evaluate the deformation mechanisms by quantifiable parameters. In the case that the component's deformation was outside at least one the prescribed limits, the component was deemed to be deformed.

The definition of specific dimensional accuracy and tolerances, respectively, was not the main focus of the study, but rather the demonstration of general deformation mechanisms.

2.5.1. *Criterion 1 – angle accuracy*

The angles of the top surface and the side surface must be in the range of 90° ± 1° The angles (∢) were measured at 0°/90°/180°/270° relative to the top surface. The same was applied for the angles of the bottom/side surface. In total, this resulted in eight angle measurement points, illustrated in Fig. 4. The purpose of this criterion is to validate the swelling and distortion of the part, with particular emphasis on the bottom-to-side and top-to-side surfaces, respectively. The process guarantees isotropic shrinkage with a constant angle ratio.

$$\measuredangle_{max} = 90\,^{\circ} \pm 1\,^{\circ} \tag{1}$$

2.5.2. *Criterion 2 – maximum height distance*

The second criterion was the maximum height distance (Hd), defined as the distance between the highest and lowest point. The mean value of the height for each part and processing step was determined as described in 2.4. The maximum height distance, shown in Eq. (2) must be in the range of the measured mean value ± 10 % of it. The maximum height distance was determined by scanning the part in the xz-plane and in the yz-plane as illustrated in Fig. 5. This criterion was defined to detect deformations characterized by denting or saddle-like distortion and to validate the planarity of the bottom-to-top layer.

$$Hd_{max} = Hd_{mean} \pm (0.1 * Hd_{mean}) \tag{2}$$

2.5.3. *Criterion 3 – ratio of maximum distance in the xz-plane and yz-plane*

The third criterion is based on the ratio of the maximum diameter distance relative to the xz-/yz-plane and focused on the maximum diameter distance as illustrated in Fig. 6 to determine the circularity. It was defined as the ratio of the maximum distance in the xz-plane (y’) and the yz-plane (x’) and must be in the range of 0.95 to 1.05 as shown in Eq. (3).

The third criterion was established with the objective of verifying the presence of circularity and detecting elliptic deformations.

$$D_{Ratio} = \frac{x'}{y'} = 1 \ \pm 0.05 \tag{3}$$

2.5.4. *Criterion 4 – volume shrinkage*

The last criterion ensured shrinkage of the component, due to pyrolysis and the gaseous decomposition products released in this process-step. This criterion, shown in Fig. 7, was instrumental to ensure dimensional compliance, thereby preventing unwanted swelling of the component. The width (w), length (l) and height (h) of the CFRP must be higher than in the final CMC state.

$$w_{CFRP} \geq w_{CMC} \tag{4}$$

$$l_{CFRP} \geq l_{CMC} \tag{5}$$

$$h_{CFRP} \geq h_{CMC} \tag{6}$$

2.6. *Simulation*

A finite element analysis package (ANSYS 2021 R2) was used to qualitatively predict different deformation mechanisms depending on the crucial printing and slicing parameters, like infill and printing direction of the part and the single layers. Especially pyrolysis, with its associated anisotropic shrinkage, combined with the release of gaseous decomposition products, can cause massive deformation of the component due to internal stresses. The printing direction was modeled by splitting up the model into multiple sections with corresponding anisotropic properties.

The heat-up was simulated using the transient thermal ANSYS package. All surfaces except for the bottom surface were subjected to convective heating up to 330 °C. The resulting strain was processed using the static structural package, with the inner ring fixed to ensure determinacy. The dependence of the printing direction on the deformed shape was modeled using anisotropic property values for the Young's modulus, shear modulus und coefficient of thermal expansion. The used values were based on PEEK (40 % carbon fiber) in the included materials library. The resulting deformation enabled a qualitative prediction of the printed part's shape.

2.7. *3D-Scan*

The scan was performed by a 3D-Scanner (CMM VL-500, Keyence, Germany) and the corresponding software. The gear wheels were centered in the scanner with the top upside and the scan cycle was composed of 12 single scans. After each scanning step the gear wheels were rotated by 30° Finally, the part was completely scanned. Afterwards, the gear wheels were flipped and the bottom side was scanned. The bottom and top scans were then merged with the software, by choosing specific reference areas and points, as shown in Fig. 8. The correct merging was proven by comparison with the geometry data measured by caliper.

3. Results and discussion

3.1. *Thermal decomposition during pyrolysis*

Pyrolysis is the key transformation step in the manufacture of CMC from PEEK-based CFRP. During this process, the PEEK matrix thermally decomposes and is converted into an amorphous carbon matrix. The main decomposition occurs in the temperature range between approximately 575 - 650 °C, accompanied by the release of a variety of gaseous decomposition products, including CO, CO_2, phenol, 4-phenoxyphenol, and 1,4-diphenoxybenzene [25,26].

The fundamental mechanisms governing this polymer-to-carbon conversion have been extensively described in the literature, particularly for phenolic resin-based CFRP systems. Although the precursor

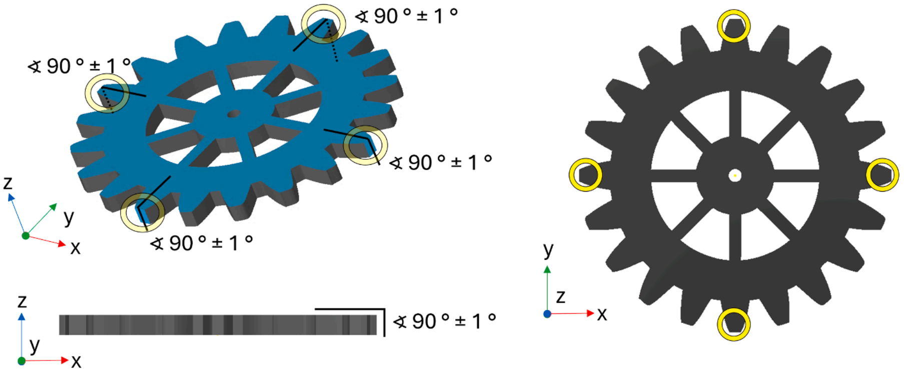

Fig. 4. Dimensional stability criterion 1 - Angle measurements of the top/bottom surface and the side surfaces at 0°/90°/180°/270°.

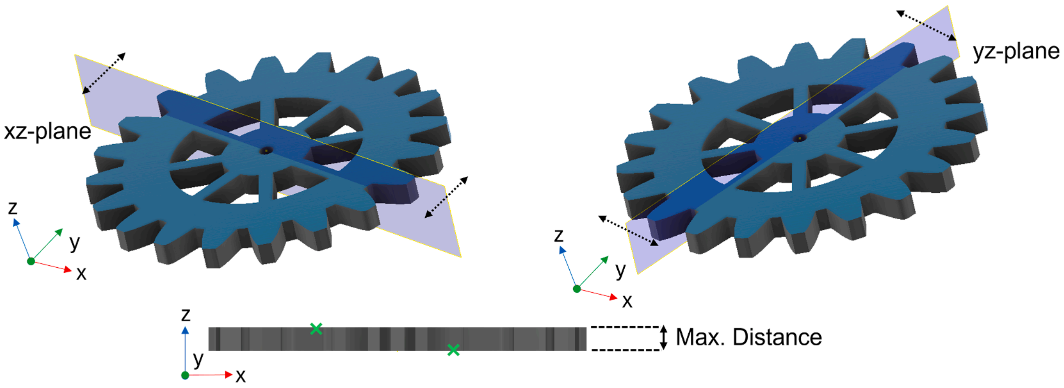

Fig. 5. Dimensional stability criterion 2 – Determination of the maximum height distance by scanning the xz-/yz-plane.

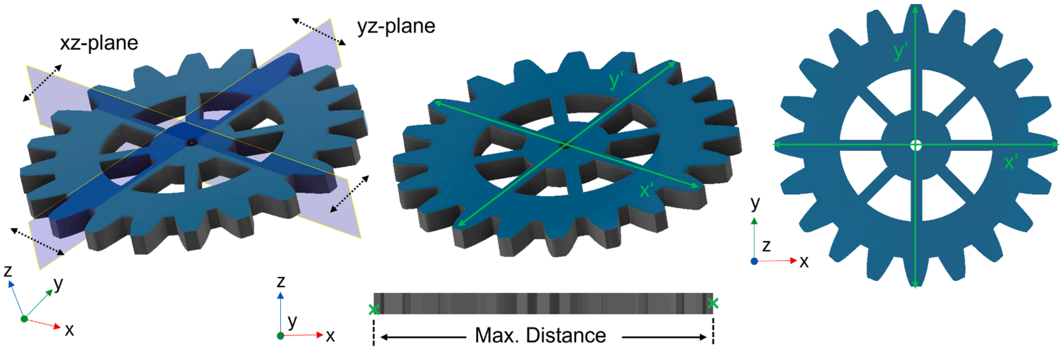

Fig. 6. Dimensional stability criterion 3 – Ratio of maximum distance in the xz-/yz-plane.

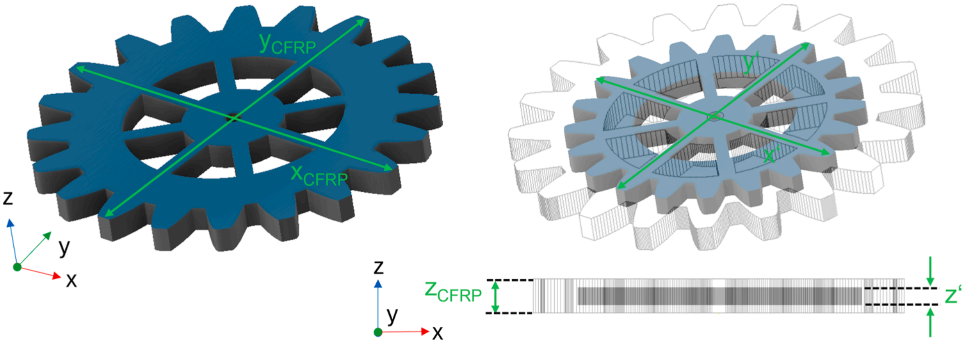

Fig. 7. Dimensional stability criterion 4 – Volume shrinkage of the component during the modified LSI-process.

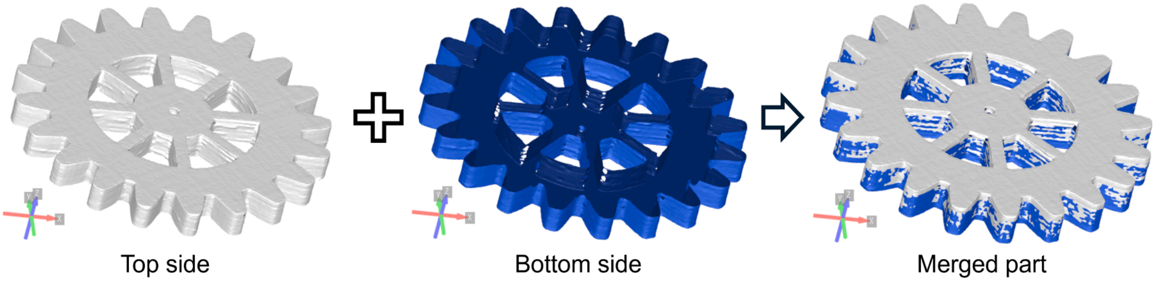

Fig. 8. Exemplary merging of the top and bottom scan to the final part.

materials differ, the underlying phenomena, namely matrix shrinkage, gas evolution, and the necessity for efficient gas transport, are generally the same for the PEEK-based CFRP investigated in this study.

As the polymer matrix transforms into amorphous carbon, it undergoes a substantial increase in density, resulting in significant volumetric shrinkage. In contrast, the carbon fibers remain dimensionally stable, particularly in their longitudinal direction. This mismatch generates high residual stress within the composite [27,28]. Simultaneously, the release of large amounts of gaseous decomposition products can locally induce volumetric expansion if gas evacuation is hindered.

The combined effects of matrix shrinkage, internal gas pressure, and the mechanical constraint imposed by carbon fibers lead to the development of a complex crack network [28,29]. A controlled degree of microcracking is beneficial, as it facilitates subsequent silicon infiltration. However, excessive crack growth, especially in the form of macroscopic delamination between laminate layers, represents a critical defect that severely compromises the mechanical integrity and reliability of the final component [30].

Achieving dimensional stability during pyrolysis therefore requires careful control of these interacting mechanisms. In particular, gaseous decomposition products must be able to escape without generating excessive internal pressure, deformation, or structural failure.

3.2. *Influence of porosity and voids on the release of gaseous decomposition products*

As mentioned in the section before, the gaseous decomposition products are required to escape ensuring shape stability for the component. Therefore, the porosity and voids are key factors for the gas transport.

In FDM-printed parts, three levels of porosity can be distinguished as shown in Fig. 9:

1. Intra-bead porosity: Microscopic pores within the filament itself, often caused by trapped moisture that evaporates during heating [16].
2. Inter-bead voids (gaps): Triangular or diamond-shaped channels that form between the printed strands of the layers [16,31,32].
3. Macroporosity (infill): Intended voids defined by the infill density and pattern [16,33].

The connectivity of these pores determines the component's permeability. Gases generated internally through pyrolysis must travel through this structure to reach the surface to escape. The path length and resistance depend directly on the tortuosity of the structure [34]. The intra-bead voids are negligible for the gas escape, whereas the larger inter-bead voids as well as the macroporosity function as gas transport channels. These can be specifically adjusted by printing parameters, like infill, printing pattern, top layers and wall layers.

3.3. *3D-Scan*

As mentioned in Section 2.7, the scanned part was merged by two separate scans of the top and bottom side, respectively. To ensure a correct final merged part, the geometry of the 3D-scanned part was compared with the geometry data measured by caliper and is illustrated in Fig. 10.

On the left side, the diameters are shown, whereas the right graphic shows the height values. The heights and diameters shown are close to the same values for each process step and are within the accuracy of the respective measurement methods, confirming the 3D-Scan as a valid method for shape analysis. The values given belong to the gear wheel with an infill of 80 % and a quasi-isotropic layer structure. In Table 1 the values, including standard deviations, are listed.

3.4. *General deformation mechanisms*

The manufacturing of CMC based on material extrusion technology revealed three general deformation mechanisms, which are illustrated in Fig. 11, where the term 'deformation' includes any geometric change in shape. The deformation mechanisms are subdivided due to their cause and the influencing factors and are discussed in the following sections. The most critical process step was identified as pyrolysis. This results from exceeding the melting temperature of PEEK, followed by the conversion of the polymer matrix into amorphous carbon and the subsequent formation of a porous C/C-body.

3.4.1. *Volume changing effects (unavoidable)*

The first deformation mechanism concerned volume changing effects of the part, illustrated in Fig. 12. The reason for these effects was the **shrinkage** during pyrolysis due to the conversion of the polymeric matrix, with the release of gaseous decomposition products, into a carbon matrix. As often described [35,36] fibers hinder the shrinkage of the matrix during pyrolysis. Thus, this effect can be influenced by the printing direction, because the fibers were aligned in printing direction due to the rheological conditions and the shear forces during the printing process. This leads to anisotropic shrinkage, with the highest shrinkage in z-direction, because the fibers can only be aligned in the planar x-y-directions. However, this enables the possibility to minimize the shrinkage in x-y-direction, by printing with quasi-isotropic layer structures. This deformation effect is not avoidable and has to be considered when designing the part.

3.4.2. *Distortion based on the fiber architecture (avoidable)*

The deformation mechanisms summarized by the term “distortion” are shown in Fig. 14. Effects of this category are also related to shrinkage and occur during pyrolysis. However, not the shrinkage itself, but deformation mechanisms based on internal stresses caused by the shrinkage. As the fibers are aligned in printing direction in combination with the hindering of shrinkage of the matrix caused by the fibers the

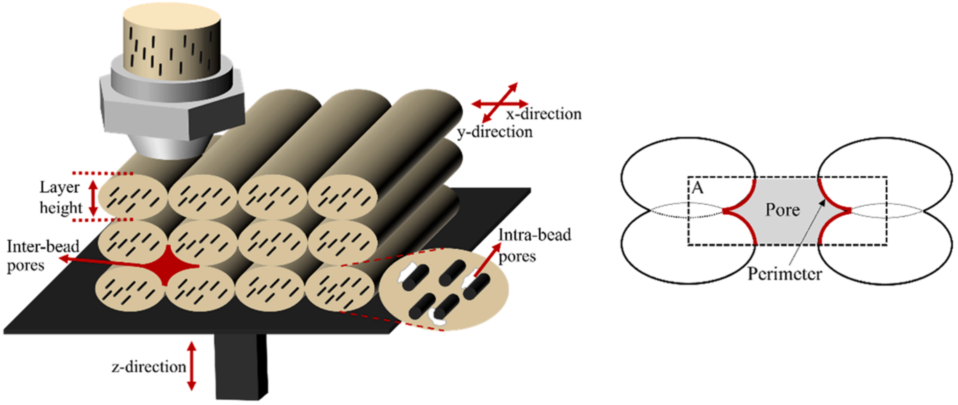

Fig. 9. Types of porosity and voids: Intra-bead voids in the filament, inter-bead voids between the single printed strands and the macroporosity resulting from low infills and the printing pattern [16].

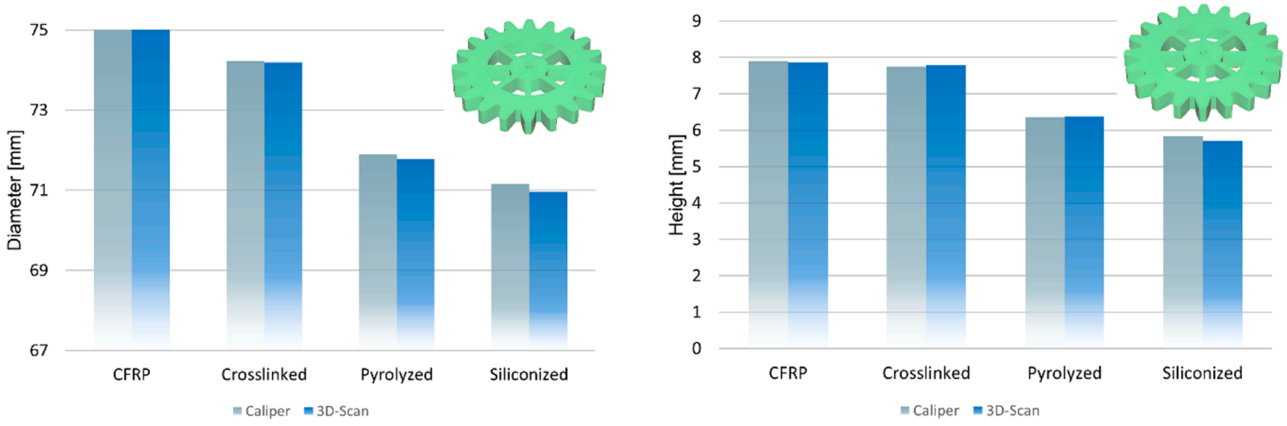

Fig. 10. Comparison of the diameter and the height of the gear wheel with 80 % infill and a quasi-isotropic layer structure over the whole process, measured by caliper vs. 3D-scan.

Table 1
Comparison of the diameter and the height measured by caliper and 3D-Scan.

	Ø [mm]		Height [mm]	
	Caliper	3D-Scan	Caliper	3D-Scan
CFRP	75.15 ± 0.13	75.09 ± 0.06	7.90 ± 0.03	7.85 ± 0.05
Crosslinked	74.23 ± 0.10	74.19 ± 0.08	7.75 ± 0.02	7.79 ± 0.04
Pyrolyzed	71.89 ± 0.07	71.78 ± 0.09	6.35 ± 0.04	6.37 ± 0.07
Siiconized	71.15 ± 0.07	70.96 ± 0.05	5.84 ± 0.05	5.70 ± 0.03

printing pattern and the layer structure are the key factors for this deformation mechanism. To underline the resulting internal stresses caused by the anisotropic shrinkage due to the aligned fibers, the occurring distortion is illustrated in Fig. 13 with an asymmetrical layer structure. The upper half of the sample was printed in 0° direction and the lower half in 90° direction, leading to the shown distortion during pyrolysis due to anisotropic shrinkage caused by internal stresses based on the fiber orientation and the printing, respectively.

These deformation mechanisms result from an anisotropic or asymmetrical layer structure, leading to anisotropic shrinkage due to the hindering of shrinkage by the fibers aligned in the printing direction. These ‘design-related’ deformation effects are avoidable by using an **isotropic** and **symmetrical** layer structure.

3.4.3. *Change and loss of shape (avoidable)*

The third subcategory includes any kind of change or loss of shape of the part, exemplary shown in Fig. 15. There are several reasons for this kind of deformation, expressed in melting, swelling or even bursting of the part. First, it is affected by the **thermally induced crosslinking**. Insufficient crosslinking, attributable to inadequate annealing time or temperature, results in (partial) remelting of the part during pyrolysis [12,17]. Especially swelling or bursting of the parts were caused by insufficient release of the gaseous decomposition products during pyrolysis, as discussed in Sections 3.1 and 3.2. This can be avoided by creating an open pore channel system due to a reduced **infill** density to avoid the contact of the single printed strands within each layer, as. Furthermore, the part should be printed without a closed **top layer** to support the release of the gaseous decomposition products. Additionally, the moisture absorbed from the air humidity in the used filaments influences the microstructure of the part, leading to a 'smeared' microstructure. This hinders the release of gaseous decomposition products and shifts the thermal conditions for thermally induced crosslinking. Insufficient crosslinking of the component can result from this, which can lead to remelting [14].

3.5. *Shape stability criteria*

The analysis of the previously defined four shape stability criteria are listed in Tables 2–7. The four criteria were listed in the lines, whereby the eight angle determinations were split between the top and bottom side. For better visual detectability each data point was marked with a green tick or a red cross depending on the compliance or noncompliance of the criterion. Moreover, the CAD model and final scanned part were attached to the right side of the tables.

The gear wheel shown in Table 2 was not thermally crosslinked, resulting in remelting during pyrolysis and swelling due to the gaseous decomposition products. Regarding the shape stability criteria, it failed in three out of four criteria.

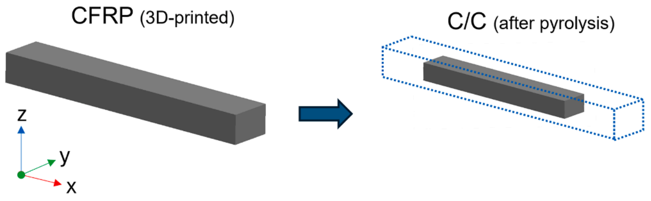

Fig. 12. Scheme of volume changing effects, caused by shrinkage during pyrolysis.

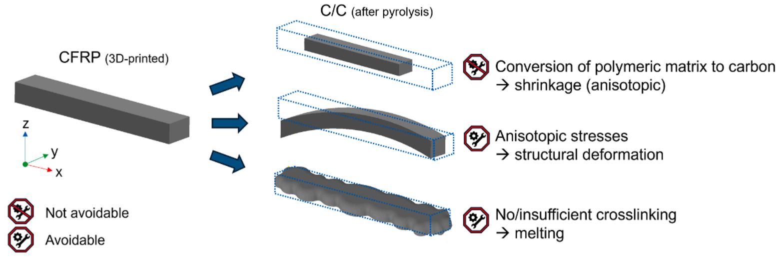

Fig. 11. Categories of three deformation mechanisms occurring during the processing (AM + LSI) based on thermoplastic CFRPs.

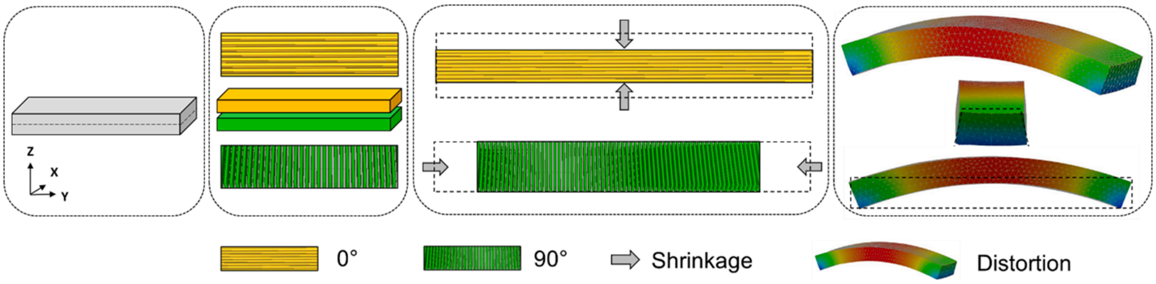

Fig. 13. Example for an asymmetrical layer structure causing distortion in the pyrolyzed part, due to anisotropic shrinkage.

The gear wheel illustrated in Table 3 was printed with 80 % infill, in a symmetric, quasi-isotropic layer structure of [0°, 90°, 45°, 135°, 60°, 150°, 30°, 120°]$_n$, without top and bottom layers. This resulted in complete fulfillment of each criterion, thus in a shape stable processing of the component.

The gear wheel in Table 4 was split in the middle and printed in 0° printing direction for the lower half and 90° printing direction for the upper half. This led to deformation due to anisotropic shrinkage during pyrolysis. The angle accuracy as well as the maximum height difference criteria failed as a result.

Additionally to the quantitative analysis of the shape stability criteria in Table 2 - 7, a visual analysis for the height difference between the CAD model and the final processed component was carried out. According to the listed gear wheels in Tables 2–7, the order of the visual

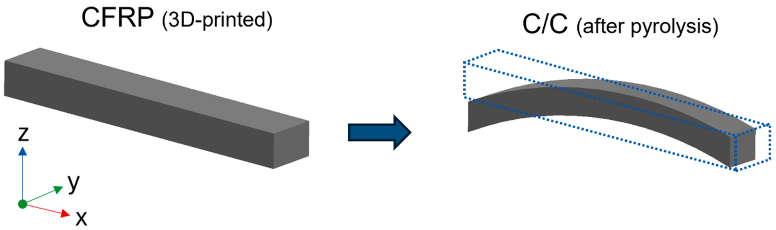

Fig. 14. Scheme of distortion due to internal stresses caused by anisotropic layer/asymmetric layer structures during pyrolysis.

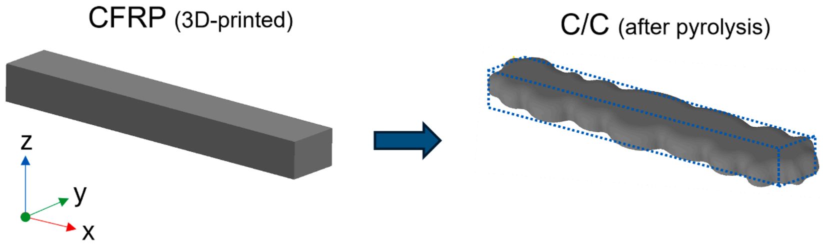

Fig. 15. Scheme of change/loss of shape, caused by shrinkage during pyrolysis.

Table 2
Analysis of the four defined shape stability criteria for the not crosslinked gear wheel, revealing shape deformation.

Criteria				0°	90°	180°	270°	Criterion check
	1	∢ [°]	Top	101,90 ×	91,70 ×	104,10 ×	92,60 ×	✓: 89° ≤ ∢ ≤ 91°
			Bottom	89,90 ✓	107,60 ×	103,20 ×	83,30 ×	
	2	ΔH	[mm]	15,87 ×				✓: ΔH_{mean}: 14.15 mm 12.735 ≤ ΔH ≤ 15.565
	3	x'/y'	[-]	1,02 ✓				✓: 0.95 ≤ x'/y' ≤ 1.05
	4	ΔV	[mm]	Ø [mm] 78,86 ×		Height [mm] 14,15 ×		✓: Ø < 75 mm Height < 8 mm

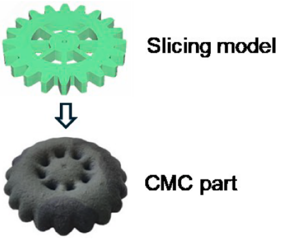

1 Angle accuracy
2 Maximum height distance of the mean value of the height distance
3 Ratio of max. distance in the xz-/yz-plane
4 Volume shrinkage

Table 3

Analysis of the four defined shape stability criteria for the idealized gear wheel, revealing shape stability.

					0°	90°	180°	270°	Criterion check
Criteria	1	∢	[°]	Top	90,10 ✓	89,50 ✓	90,20 ✓	90,30 ✓	✓: 89° ≤ ∢ ≤ 91°
				Bottom	89,90 ✓	90,40 ✓	89,80 ✓	89,70 ✓	
	2	ΔH	[mm]		6,02 ✓				✓: ΔH_{mean}: 5.70 mm 5.13 ≤ ΔH ≤ 6.27
	3	x'/y'	[-]		0,99 ✓				✓: 0.95 ≤ x'/y' ≤ 1.05
	4	ΔV	[mm]		Ø [mm] 70,96 ✓		Height [mm] 5,70 ✓		✓: Ø < 75 mm Height < 8 mm

1 Angle accuracy
2 Maximum height distance of the mean value of the height distance
3 Ratio of max. distance in the xz-/yz-plane
4 Volume shrinkage

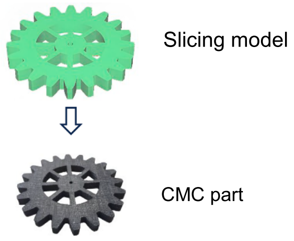

Table 4

Analysis of the four defined shape stability criteria for the split gear wheel, revealing shape deformation.

					0°	90°	180°	270°	Criterion check
Criteria	1	∢	[°]	Top	97,80 ✗	83,20 ✗	100,00 ✗	81,40 ✗	✓: 89° ≤ ∢ ≤ 91°
				Bottom	82,70 ✗	97,40 ✗	79,50 ✗	98,00 ✗	
	2	ΔH	[mm]		9,51 ✗				✓: ΔH_{mean}: 5.79 mm 5.211 ≤ ΔH ≤ 6.369
	3	x'/y'	[-]		1,00 ✓				✓: 0.95 ≤ x'/y' ≤ 1.05
	4	ΔV	[mm]		Ø [mm] 71,88 ✓		Height [mm] 5,79 ✓		✓: Ø < 75 mm Height < 8 mm

1 Angle accuracy
2 Maximum height distance of the mean value of the height distance
3 Ratio of max. distance in the xz-/yz-plane
4 Volume shrinkage

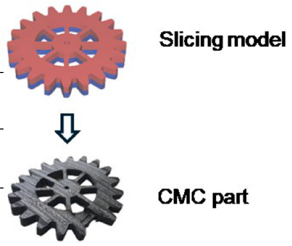

analysis illustrated in Fig. 16& 17 was kept the same. The lower image showed in each case the overlay of the processed, scanned and merged gear wheel (dark grey) and the adjusted CAD model (white). The adjusted CAD model was calculated, as described in Section 3.7, after the deduction of shrinkage from the CFRP to the CMC part. Thus, the adjusted CAD model was set to 5.91 mm in height and 71.01 mm in diameter. For better comparison, the scale bar of height difference was set the same level for each gear wheel. The visualization of the height difference confirmed and underlined the results of the shape stability criteria.

The gear wheel in Table 5 was printed in 0° printing direction, resulting in anisotropic shrinkage during pyrolysis. Besides the failed criterion 1 and 2, this gear wheel failed especially at criterion 3, the ratio of length and width.

The gear wheel in Table 6 was printed graded with four different infills of 100 % at the starting layer and finished with 70 % infill at the top of it. This led to bulging of the part due to different shrinkage hinderance caused by the decrease in fiber volume content from the bottom to the top side. The deformation of the part is quantified by failing criteria 1 and 2.

The gear wheel in Table 7 was printed with top and bottom layers. The tightness of the top layers avoided the release of the gaseous decomposition products during pyrolysis, resulting in partially swelling and bubble-like structures on the top layer, visualized in Fig. 17 (right side).

3.6. Simulation results

Based on the previously described assumptions, it was possible to simulate the deformation mechanisms qualitatively. Fig. 18 shows that the simulated results fit well with the real processed parts, particularly regarding the deformation mechanisms, provided the correct boundary conditions are known. That enables deformation predictions as a function of the fiber alignment and other slicing parameters, which in turn saves material, time and at least costs for the processing of different components.

During the simulated heating of the anisotropic materials, deformation occurred. As a function of the boundary conditions set, the deformations varied in the final simulated part, showing compression and tensile stresses, respectively. The upper model was split in half, and a 0°/

Table 5

Analysis of the four defined shape stability criteria for the gear wheel printed in 0°, revealing shape deformation.

Criteria				0°	90°	180°	270°	Criterion check
1	∢	[°]	Top	77,00 ✗	89,70 ✓	84,40 ✗	87,90 ✗	✓: 89° ≤ ∢ ≤ 91°
			Bottom	102,50 ✗	90,30 ✓	96,00 ✗	92,20 ✗	
2	ΔH	[mm]		9,00 ✗				✓: ΔH_{mean}: 14.15 mm 12.735 ≤ ΔH ≤ 15.565
3	x'/y'	[-]		1,12 ✗				✓: 0.95 ≤ x'/y' ≤ 1.05
4	ΔV	[mm]		Ø [mm] n.a. ✓		Height [mm] 5,87 ✓		✓: Ø < 75 mm Height < 8 mm

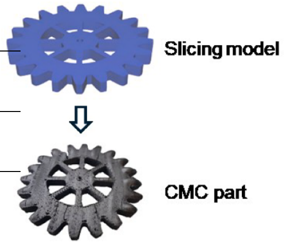

1 Angle accuracy
2 Maximum height distance of the mean value of the height distance
3 Ratio of max. distance in the xz-/yz-plane
4 Volume shrinkage

Table 6

Analysis of the four defined shape stability criteria for the graded gear wheel, revealing shape deformation.

Criteria				0°	90°	180°	270°	Criterion check
1	∢	[°]	Top	77,20 ✗	76,50 ✗	75,80 ✗	78,60 ✗	✓: 89° ≤ ∢ ≤ 91°
			Bottom	102,30 ✗	103,40 ✗	104,70 ✗	101,50 ✗	
2	ΔH	[mm]		7,38 ✗				✓: ΔH_{mean}: 14.15 mm 12.735 ≤ ΔH ≤ 15.565
3	x'/y'	[-]		1,00 ✓				✓: 0.95 ≤ x'/y' ≤ 1.05
4	ΔV	[mm]		Ø [mm] 71,87 ✓		Height [mm] 5,46 ✓		✓: Ø < 75 mm Height < 8 mm

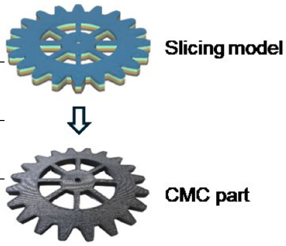

1 Angle accuracy
2 Maximum height distance of the mean value of the height distance
3 Ratio of max. distance in the xz-/yz-plane
4 Volume shrinkage

90° printing direction was modeled by selecting an appropriate anisotropic material. The difference in CTE resulted in a saddle-like distortion. The lower model had isotropic material properties. The uneven heating up led to bowl-shaped deformation.

The analysis is limited to qualitative predictions, since many assumptions must be made, and some real effects, like creeping, are not included in the static structural analysis. Hence, the predicted amount of deformation was significantly smaller than that of the real parts and qualitative results are not included in the analysis.

3.7. *Shrinkage and reverse geometry calculations*

The investigations and results enabled the reverse geometry calculations for the final part dimensions. In case of isotropic shrinkage of the part, a preliminary calculation was also carried out by the carbon yield of PEEK after pyrolysis in combination with the known fiber volume content. However, the anisotropic shrinkage due to the hindering of shrinkage caused by the fibers aligned in the x-y-direction prevented a detailed pre-calculation of the shrinkage for each direction.

The determined shrinkage in the x-y and z-direction, respectively, after each process step is illustrated in Fig. 19. It was observed that the highest shrinkage occurred during pyrolysis due to the decomposition of the polymeric matrix. Furthermore, the total shrinkage from CFRP to the final C/C-SiC of 26.13 % in the z-direction was much higher than the measured 5.32 % in x-y-direction. Finally, it was possible to calculate the required ‘oversize’ for the CFRP component with the formula of Eq. (7)–9. The calculated values x_{CFRP}, y_{CFRP}, and z_{CFRP} represented the percentage oversize, which have to be added when printing the CFRP, based on the real percentage shrinkage values $x_{shrinkage}$, $y_{shrinkage}$, and $z_{shrinkage}$.

$$x_{CFRP} = \left(\left(\frac{100}{100 - x_{shrinkage}}\right) - 1\right) * 100\ \% \tag{7}$$

$$y_{CFRP} = \left(\left(\frac{100}{100 - y_{shrinkage}}\right) - 1\right) * 100\ \% \tag{8}$$

Table 7

Analysis of the four defined shape stability criteria for the gear wheel printed with top and bottom layer, revealing shape deformation.

Criteria			0°	90°	180°	270°	Criterion check
1	∢ [°]	Top	88,90 ×	89,90 ✓	87,70 ×	88,70 ×	✓: 89° ≤ ∢ ≤ 91°
		Bottom	91,20 ×	89,90 ✓	92,10 ×	91,50 ×	
2	ΔH	[mm]	8,32 ×				✓: ΔH_{mean}: 14.15 mm 12.735 ≤ ΔH ≤ 15.565
3	x'/y'	[-]	1,00 ✓				✓: 0.95 ≤ x'/y' ≤ 1.05
4	ΔV	[mm]	Ø [mm] 72,02 ✓		Height [mm] 5,83 ✓		✓: Ø < 75 mm Height < 8 mm

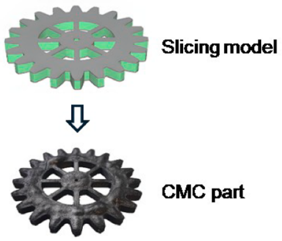

1 Angle accuracy
2 Maximum height distance of the mean value of the height distance
3 Ratio of max. distance in the xz-/yz-plane
4 Volume shrinkage

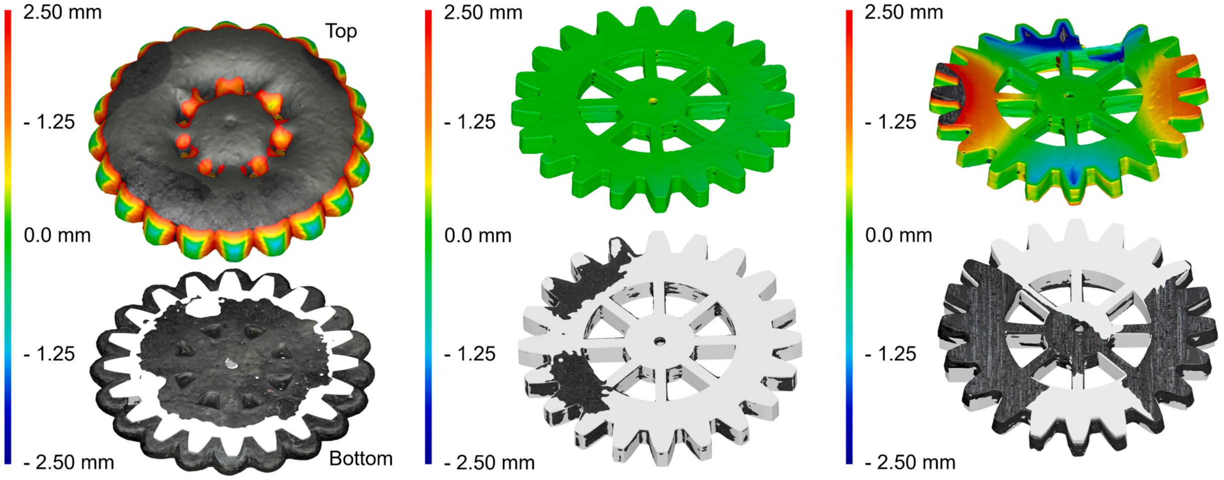

Fig. 16. Height difference of the gear wheels according to the different printing parameters.

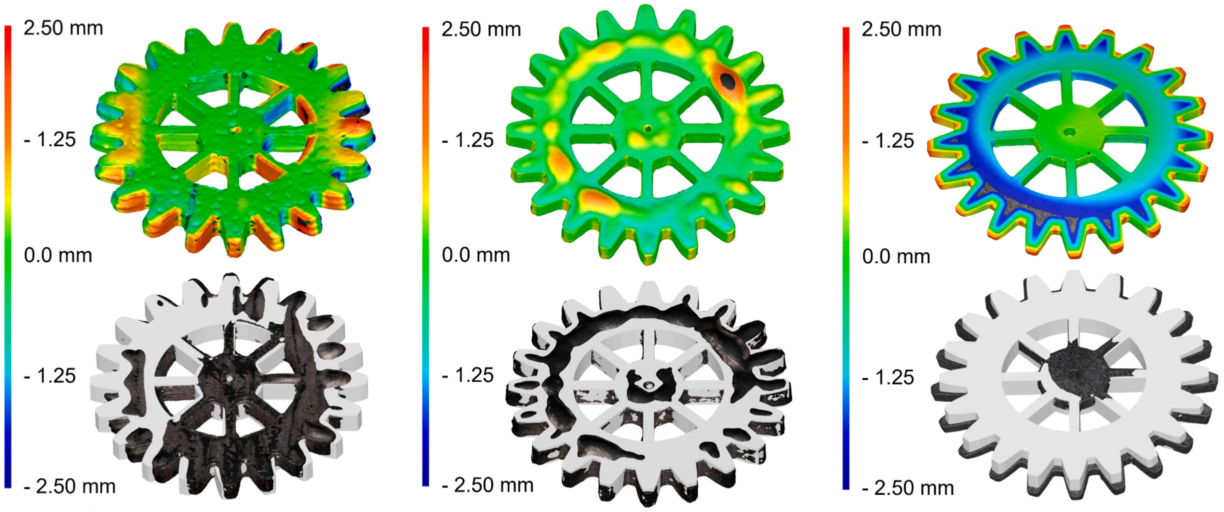

Fig. 17. Height difference of the gear wheels according to the different printing parameters.

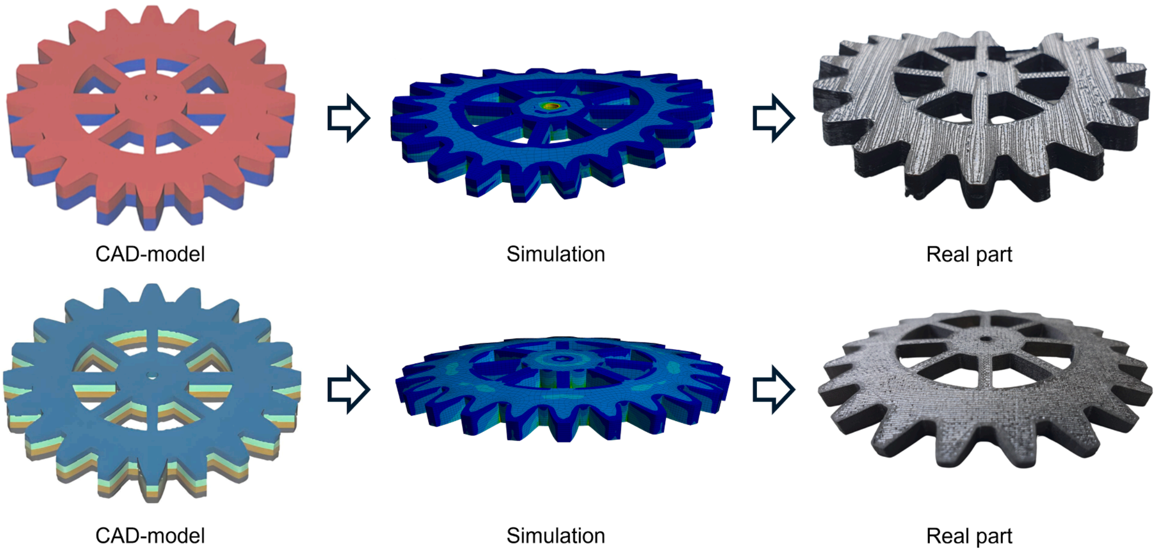

Fig. 18. Exemplary gear wheels; sliced version including infill and layer structure (left), simulation (middle), real siliconized part (right).

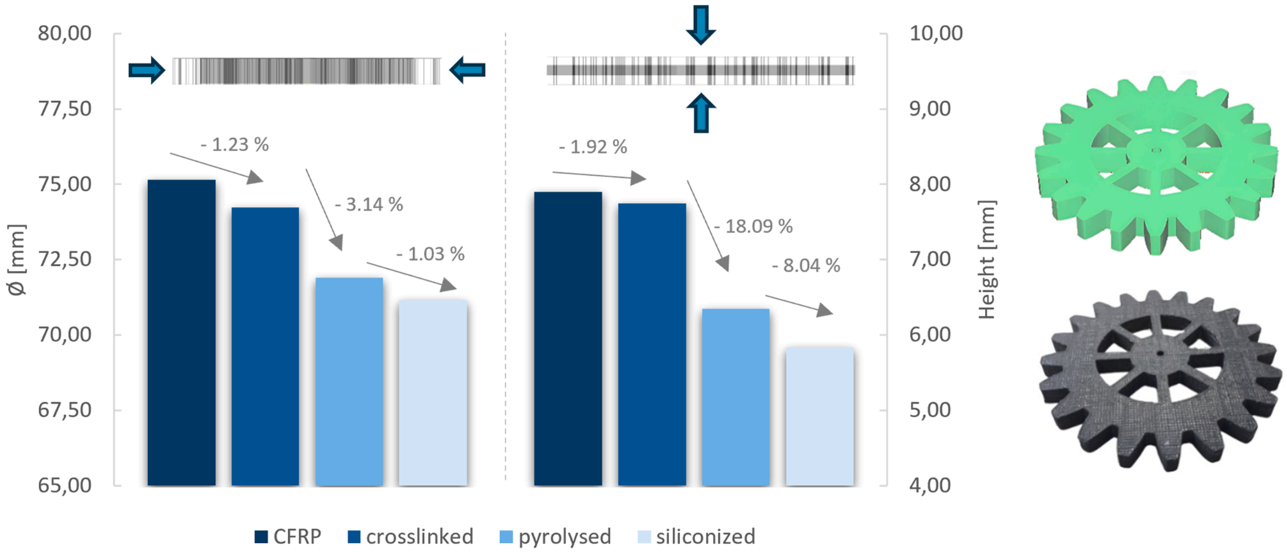

Fig. 19. Shrinkage of the “ideal” printed gear wheel in x-y (left) and z-direction (right), respectively.

$$z_{CFRP} = \left(\left(\frac{100}{100 - z_{shrinkage}}\right) - 1\right) * 100\ \% \tag{9}$$

Based on that calculation the CAD model must have a height of 10.83 mm, corresponding to 135 % of the target height and a diameter of 79.21 mm, corresponding to 105 % of the target diameter, to get the final

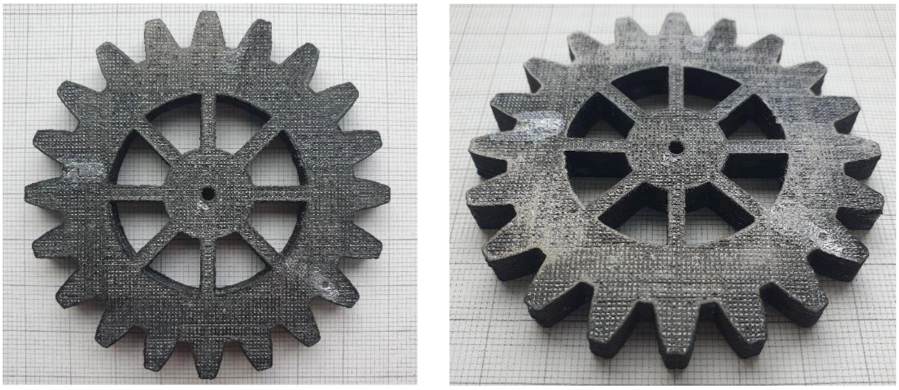

Fig. 20. Final processed pre-oversized gear wheel placed on millimeter paper for better visualization of the geometry.

geometry of 8 × 75 mm^2 in height in diameter for the CMC state. In Fig. 20 the siliconized gear wheel with the precalculated values is demonstrated. The final geometry was determined with 75.28 mm in diameter and 7.79 mm in height. This was in excellent accordance with the target values of 75 × 8 mm^2 and demonstrated the efficacy of the reverse calculation method.

4. Summary and conclusion

The aim of this study was to investigate and quantify deformation mechanisms occurring during the additive manufacturing and conversion of carbon fiber reinforced PEEK components into C/C-SiC via the liquid silicon infiltration (LSI) process. The results demonstrated that process-induced deformation is influenced by a complex interplay of material properties, slicing parameters, and process conditions across the manufacturing chain.

The most obvious shape changing effect was the shrinkage-related deformation during pyrolysis as an unavoidable but predictable mechanism. The transformation of the thermoplastic matrix into a porous carbon matrix, combined with anisotropic fiber orientation, led to characteristic volume changing effects - particularly a significantly higher shrinkage in the z-direction compared to x-y, due to the planar alignment of the short carbon fibers during printing process. This directional dependency underlines the importance of oversizing strategies in CAD design, which were successfully implemented and validated through dimensional measurements and FEM simulation for qualitative validation.

In contrast, distortion due to asymmetric or anisotropic slicing strategies was shown to be an avoidable deformation mechanism. The use of non-uniform layer orientations or abrupt changes in infill density led to internal stress during pyrolysis, resulting in warping or denting of the final component. These findings emphasize the critical role of slicing strategies in ensuring shape fidelity. Gear wheels manufactured with a quasi-isotropic and symmetric layer structure achieved high dimensional stability and fulfilled all defined shape stability criteria.

Furthermore, the results revealed that inadequate gas release during pyrolysis can cause severe shape changes, including swelling or bursting. This was particularly evident in components with closed top layers or insufficient infill porosity. In addition, insufficient thermal crosslinking of the PEEK matrix led to partial remelting during pyrolysis, further compromising dimensional integrity. These phenomena highlight the necessity of well-controlled thermal pretreatment and moisture management of the filament material to ensure reliable crosslinking and prevent microstructural defects.

The dimensional stability criteria introduced in this study - angle accuracy, maximum height distance, circularity, and volume shrinkage - proved effective for objectively quantifying deformation even in geometrically complex parts. Their application, together with FEM simulations, enabled the classification of deformation types and the correlation with process parameters. The simulation models successfully predicted the general trends of deformation and illustrated the potential of predictive process design to minimize post-processing efforts.

However, the dimensional stability criteria defined in this study are specific to the material used, process and gear wheel component. The deformation and shrinkage mechanisms identified in this study are generally applicable and represent fundamental effects that also occur in other fiber-reinforced thermoplastic-based components. The resulting dimensional changes and deformation behavior are significantly influenced by parameters such as the geometry, printing direction, infill, fiber type, fiber volume content and fiber length, which will massively influence the shrinkage and deformation mechanisms of the component. Consequently, while the underlying mechanisms remain broadly valid, their individual impact must be reassessed and analyzed separately for each material–component–process combination.

Data availability

Data will be made available on reasonable request to the corresponding author.

CRediT authorship contribution statement

Wolfgang Freudenberg: Writing – original draft, Visualization, Project administration, Methodology, Investigation, Data curation, Conceptualization. **Felix Werner:** Writing – review & editing, Software, Data curation. **Max Friedel:** Writing – review & editing, Software, Data curation. **Nico Langhof:** Writing – review & editing, Supervision. **Holger Ruckdäschel:** Writing – review & editing. **Stefan Schafföner:** Writing – review & editing, Supervision.

Declaration of competing interest

The authors declare that they have no known competing financial interests or personal relationships that could have appeared to influence the work reported in this paper.

Funding Acknowledgement

This work was funded by the Deutsche Forschungsgmeinschaft (DFG, German Research Foundation) - LA 4649/1-1 and by the Open Access Publishing Fund of the University of Bayreuth.

References

[1] I.-M. Low (Ed.), Advances in Ceramic Matrix Composites, WP Woodhead Publishing an imprint of Elsevier, Duxford, Cambridge, MA, Kidlington, 2018.

[2] H.M. Azad, M.Z. Rahman, Ceramic matrix composites with particulate reinforcements—Progress over the past 15 years, in: S. Hashmi (Ed.), Comprehensive Materials Processing, 2nd edition, Elsevier, Amsterdam, Netherlands, 2024, pp. 395–408.

[3] C. Rajesh, Applications of ceramic matrix composites, in: I.H. Mondal (Ed.), Technical Organic and Inorganic Fibres from Natural Resources, 1stst ed., Elsevier Science & Technology, San Diego, 2025, pp. 741–763. https://doi.org/10.1016/B978-0-443-15459-1.00017-6.

[4] F. Zivic, N. Busarac, S. Milenkovic, N. Grujović, in: D. Brabazon (Ed.), General Overview and Applications of Ceramic Matrix Composites (CMCs), Encyclopedia of Materials: CompositesElsevier, San Diego, 2021, pp. 3–19. https://doi.org/10.1016/B978-0-12-819724-0.00056-2.

[5] M.F. Wani, J.K. Katiyar, R. Sehgal, Classification and high-temperature applications of ceramics, in: M.F. Wani, J.K. Katiyar, R. Sehgal (Eds.), High-temperature Tribology of Ceramics and Ceramic Matrix Composites, Elsevier, Amsterdam, London, Cambridge, MA, 2025, pp. 27–47. https://doi.org/10.1016/B978-0-323-91605-9.00005-8.

[6] A.P. Garshin, V.I. Kulik, A.S. Nilov, Analysis of the status and prospects for the commercial use of fiber-reinforced silicon-carbide ceramics, Refract Ind Ceram 53 (2012) 62–70, https://doi.org/10.1007/s11148-012-9463-9.

[7] H. Abu El-Hija, W. Krenkel, Cost analysis for the manufacture of C/C-SiC structural parts, in: W. Krenkel, R. Naslain, H. Schneider, W. Krenkel (Eds.), High Temperature Ceramic Matrix Composites, Wiley-VCH, Weinheim, 2006, pp. 846–851.

[8] N.P. Bansal, Handbook of Ceramic Composites, Springer US, Kluwer, Boston, MA, Boston, 2005.

[9] S. Shrivastava, D.K. Rajak, T. Joshi, D.K. Singh, D.P. Mondal, Ceramic matrix composites: classifications, manufacturing, properties, and applications, Ceramics 7 (2024) 652–679, https://doi.org/10.3390/ceramics7020043.

[10] S. Flauder, F. Wich, J. Sha, N. Langhof, W. Krenkel, S. Schafföner, Effect of thermo-mechanical and low-cycle preloading on the strength of carbon fiber-reinforced ceramic matrix composites, J. Eur. Ceram. Soc. 43 (2023) 5474–5483, https://doi.org/10.1016/j.jeurceramsoc.2023.05.037.

[11] M. Moos, C. Möhl, O. Reichert, G. Ohnemüller, N. Langhof, S. Baz, T. Opel, G. T. Gresser, S. Schafföner, Novel approach for ceramic matrix composites – Cf/PEEK hybrid yarn-based C/C-SiC, J. Eur. Ceram. Soc. 44 (2024) 130–141, https://doi.org/10.1016/j.jeurceramsoc.2023.09.005.

[12] W. Freudenberg, F. Wich, N. Langhof, S. Schafföner, Additive manufacturing of carbon fiber reinforced ceramic matrix composites based on fused filament fabrication, J. Eur. Ceram. Soc. 42 (2022) 1822–1828, https://doi.org/10.1016/j.jeurceramsoc.2021.12.005.

[13] A. Tezvergil, L.V.J. Lassila, P.K. Vallittu, The effect of fiber orientation on the polymerization shrinkage strain of fiber-reinforced composites, Dental Mater. 22 (2006) 610–616, https://doi.org/10.1016/j.dental.2005.05.017.

[14] R.J. Zaldivar, T.D. Mclouth, G.L. Ferrelli, D.N. Patel, A.R. Hopkins, D. Witkin, Effect of initial filament moisture content on the microstructure and mechanical

performance of ULTEM® 9085 3D printed parts, Addit. Manuf. 24 (2018) 457–466, https://doi.org/10.1016/j.addma.2018.10.022.

[15] P. Greil, Near net shape manufacturing of polymer derived ceramics, J. Eur. Ceram. Soc. 18 (1998) 1905–1914, https://doi.org/10.1016/S0955-2219(98)00129-0.

[16] J. Best, W. Freudenberg, N. Langhof, S. Schafföner, Processing-microstructure correlations in material extrusion additive manufacturing of carbon fiber reinforced ceramic matrix composites, Addit. Manuf. 79 (2024) 103888, https://doi.org/10.1016/j.addma.2023.103888.

[17] W. Freudenberg, F. Wich, J. Best, E. Moukhina, T. Scherzer, H. Ruckdäschel, N. Langhof, S. Schafföner, Thermo-oxidative crosslinking of carbon fiber reinforced PEEK (Polyetheretherketone) for additive manufactured ceramic matrix composites, Adv. Manufactur.: Poly. Composit. Sci. 10 (2024) 2387422, https://doi.org/10.1080/20550340.2024.2387422.

[18] DIN EN ISO 129-1:2022-02, Technische Produktdokumentation_(TPD)_- Angabe von Maßen und Toleranzen_- Teil_1: Grundlagen (ISO_129-1:2018_+ Amd_1:2020); Deutsche Fassung EN_ISO_129-1:2019_+ A1, DIN Media GmbH, Berlin, 2021.

[19] DIN EN ISO 286-1:2019-09, Geometrische Produktspezifikation_(GPS)_- ISO-Toleranzsystem für Längenmaße_- Teil_1: Grundlagen für Toleranzen, Abmaße und Passungen (ISO_286-1:2010_+ Cor_1:2013); Deutsche Fassung EN_ISO_286-1:2010_+ AC, DIN Media GmbH, Berlin, 2013.

[20] DIN EN ISO 14405-1:2017-07, Geometrische Produktspezifikation_(GPS)_-Dimensionelle Tolerierung_- Teil_1: Lineare Größenmaße (ISO_14405-1:2016); Deutsche Fassung EN_ISO_14405-1, DIN Media GmbH, Berlin, 2016.

[21] DIN EN ISO 1938-1:2016-03, Geometrische Produktspezifikation_(GPS)_-Längenprüftechnik_- Teil_1: Grenzlehren und Lehrung der Längenmaße (ISO_1938-1:2015); Deutsche Fassung EN_ISO_1938-1, DIN Media GmbH, Berlin, 2015.

[22] DIN ISO 2768-1:1991-06, Allgemeintoleranzen; toleranzen für Längen- und Winkelmaße ohne einzelne toleranzeintragung; Identisch Mit ISO_2768-1:1989, DIN Media GmbH, Berlin, 1991.

[23] DIN ISO 2768-2:1991-04, Allgemeintoleranzen; Toleranzen für Form Und Lage ohne Einzelne Toleranzeintragung; Identisch mit ISO_2768-2, Beuth Verlag GmbH, Berlin, 1989.

[24] DIN EN ISO/ASTM 52902:2023-12, Additive Fertigung_- Testkörper_-Geometrische Leistungsbewertung Additiver Fertigungssysteme (ISO/ASTM 52902:2023); Deutsche Fassung EN_ISO/ASTM 52902, DIN Media GmbH, Berlin, 2023.

[25] C.J. Tsai, L.H. Perng, Y.C. Ling, A study of thermal degradation of poly(aryl-ether-ether-ketone) using stepwise pyrolysis/gas chromatography/mass spectrometry, Rapid. Commun. Mass Spectrom. 11 (1997) 1987–1995, https://doi.org/10.1002/(SICI)1097-0231(199712)11:18<1987:AID-;CM100>3.0.CO;2-Q.

[26] P. Patel, T.R. Hull, R.E. Lyon, S.I. Stoliarov, R.N. Walters, S. Crowley, N. Safronava, Investigation of the thermal decomposition and flammability of PEEK and its carbon and glass-fibre composites, Polym. Degrad. Stab. 96 (2011) 12–22, https://doi.org/10.1016/j.polymdegradstab.2010.11.009.

[27] J. Schulte-Fischedick, M. Frie, W. Krenkel, R. Kochendrfer, M. Knig, Crack Microstructure During The Carbonization Of Carbon Fibre Reinforced Plastics To Carbon/Carbon Composites, International Committee on Composite Materials (ICCM), 1999.

[28] F. Kessel, L. Baier, N. Hensch, M. Frieß, A. Markic, T. Bratzdrum, D. Koch, Microstructure development during pyrolysis of wet-laid nonwoven-based CFRP for the manufacturing of ceramic matrix composites (CMC), Open Ceramics 23 (2025) 100835, https://doi.org/10.1016/j.oceram.2025.100835.

[29] J. Schulte-Fischedick, A. Zern, J. Mayer, M. Rühle, H. Voggenreiter, The crack evolution on the atomistic scale during the pyrolysis of carbon fibre reinforced plastics to carbon/carbon composites, Composites, Part A 38 (2007) 2237–2244, https://doi.org/10.1016/j.compositesa.2007.05.004.

[30] S. Hofmann, D. Koch, Predicting the mechanical behaviour of carbon fibre reinforced silicon carbide with interlaminar manufacturing defects, MATEC Web Conferenc. 29 (2015) 00012, https://doi.org/10.1051/matecconf/20152900012.

[31] F. Pina, C.M.S. Vicente, J.J. Netto, L. Reis, Static and cyclic mechanical behavior of 3D-printed PEEK under tensile and compressive loads, Poly. (Basel) 18 (2026) 748, https://doi.org/10.3390/polym18060748.

[32] S. Garg, A. Singh, Q. Murtaza, Measuring the impact of infill pattern and infill density on the properties of 3D-printed PLA via FDM, J. Materi Eng Perform. 34 (2025) 22597–22610, https://doi.org/10.1007/s11665-025-10837-y.

[33] E. Vázquez-Silva, J.A. Pintado-Pintado, F.P. Moncayo-Matute, P.B. Torres-Jara, D. P. Moya-Loaiza, Effect of infill density on the mechanical properties of natural peek processed by additive manufacturing, Poly. (Basel) 17 (2025) 347, https://doi.org/10.3390/polym17030347.

[34] Y. Liu, A. Al-Akailah, F. Ning, Mass transport and porous structure evolution during solvent debinding of additively manufactured stainless steel, Virtual. Phys. Prototyp. 20 (2025) e2586637, https://doi.org/10.1080/17452759.2025.2586637.

[35] J. Schulte-Fischedick, S. Seiz, N. Lützenburger, A. Wanner, H. Voggenreiter, The crack development on the micro- and mesoscopic scale during the pyrolysis of carbon fibre reinforced plastics to carbon/carbon composites, Composit., Part A 38 (2007) 2171–2181, https://doi.org/10.1016/j.compositesa.2007.06.013.

[36] Y.-F. Li, J.-Y. Li, J.-Y. Syu, T.-H. Yang, S.-M. Chang, M.-Y. Shen, Mechanical behaviors of microwave-assisted pyrolysis recycled carbon Fiber-reinforced concrete with early-strength cement, Mater. (Basel) 16 (2023) 1507, https://doi.org/10.3390/ma16041507.